**VTT Technical Research Centre of Finland**

# High-performance infrared thermoelectric bolometers based on nanomembranes

Varpula, Aapo; Tappura, Kirsi; Tiira, Jonna; Grigoras, Kestutis; Viherkanto, Kai; Ahopelto, Jouni; Prunnila, Mika

*Published in:*
Photonic and Phononic Properties of Engineered Nanostructures X

*DOI:*
10.1117/12.2542194

Published: 26/02/2020

*Document Version*
Peer reviewed version

# High-performance infrared thermoelectric bolometers based on nanomembranes

Aapo Varpula*[a], Kirsi Tappura[a], Jonna Tiira[a], Kestutis Grigoras[a], Kai Viherkanto[a], Jouni Ahopelto[a], Mika Prunnila[a]
[a]VTT Technical Research Centre of Finland Ltd, Tietotie 3, FI-02150 Espoo, Finland

## ABSTRACT

The state-of-the-art infrared (IR) photodetectors are either thermal detectors (bolometers) or quantum detectors (photovoltaic and photoconductive detectors). Compared to quantum IR photodetectors, IR bolometers are slower and less sensitive but in turn, they offer lower cost without need for cooling and exotic materials (e.g. HgCdTe). Phonon/photon engineered materials offer interesting routes for enhancing room-temperature IR bolometers. We have recently demonstrated experimentally a nano-thermoelectric bolometer for long-wave IR detection. The technology utilizes efficient thermoelectric transducers based on silicon nanomembranes, which have an enhanced thermoelectric figure of merit arising from the low thermal conductivity stemming from the nano-scale thickness. For the absorption of the IR radiation the nano-thermoelectric bolometer utilizes a nanomembrane based quarter-wave resistive absorber, which is also known as the Salisbury screen. The use of nanomembranes in both the thermoelectric transducer and the absorber results in a very small thermal mass, and thereby high speed for the detector. In this article, we present an analytical model for quarter-wave resistive absorbers (i.e. Salisbury screens). It can be applied both in radio frequency (RF) and optical applications. The results of the analytical model are compared with the ones obtained with the transfer-matrix method using the optical material data available in the literature. We present also a device model of the nano-thermoelectric IR detector and estimate the full performance of this technology.

**Keywords:** infrared, uncooled detector, silicon, thermoelectric, nanomembrane, quarter-wave resistive absorber, Salisbury screen

## 1. INTRODUCTION

The state-of-the-art (SoA) infrared (IR) photodetectors are either thermal detectors or quantum detectors (photovoltaic and photoconductive detectors). Quantum IR photodetectors have high performance, but obtaining high sensitivity in, for example, thermal IR regime requires cooling and exotic materials (e.g. HgCdTe). In the IR range the most common thermal detectors are resistive and thermoelectric bolometers. The former type utilize temperature-dependent resistors to transduce the thermal signal into electric signal. Historically, the use of the term 'bolometer' has been limited to these kinds of resistive bolometers[1,2]. However, since, the term refers to the detection of optical radiation[2], we have extended the use of this term to other kinds of similar thermal detectors as well. The SoA thermoelectric bolometers employ thermocouples or thermopiles in signal transduction. Compared to quantum detectors, bolometers are typically slower and less sensitive but in turn, they offer lower cost without the need for cooling.

A thermoelectric bolometer is schematically illustrated in Fig. 2. The device consist of the optical absorber, thermoelectric transducer (i.e. p- and n-type thermoelectric materials), supporting structures, electric contacts, and readout electronics. The absorber absorbs the incident optical radiation and heats up. This results in a temperature gradient along the structure supporting the absorber above the substrate. The temperature gradient is converted into electric voltage using p- and n-type thermoelectric materials (i.e. legs) placed in/on the supporting structure. This thermal electric voltage is measured using readout electronics, which are often located in the substrate.

*aapo.varpula@vtt.fi; phone 358 40 357-1370; vttresearch.com

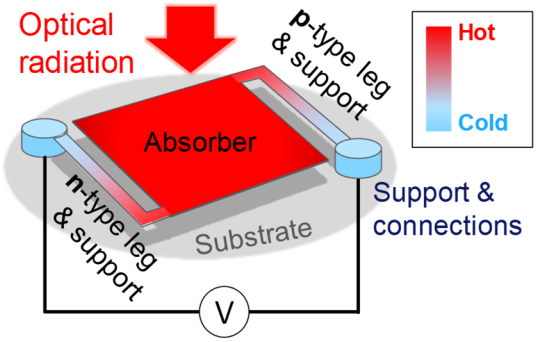


Figure 1. Schematic picture of a thermoelectric bolometer. The absorber absorbs the incident optical radiation and heats up. The resulted temperature gradient is converted into electric voltage using p- and n-type thermoelectric materials (i.e. legs) placed in/on the supporting structure.

Phonon engineered materials offer many interesting routes for enhancing the performance of IR bolometers. We have recently experimentally demonstrated that both ultra-thin single-crystalline and poly-crystalline silicon membranes work as efficient thermoelectric transducers in fast and sensitive electro-thermal detectors[3–5]. The high sensitivity of the devices originates from the increased phonon scattering when the thickness of the Si membrane is reduced, leading to reduced thermal conductivity[6]. This gives rise to the high thermoelectric figures of merit of these membranes, which, in turn, determines the detector sensitivity[4]. The speed of the devices stems from the small thermal mass of the nanomembrane.

Since the thermoelectric transducers of these nano-thermoelectric devices are based on nanomembranes, it is convenient to use nanomembranes also in the optical absorber as well. Quarter-wave resistive absorbers based on thin conductive layers provide relatively broad bandwidth and enable fast operation due to the inherently low thermal mass when integrated with vacuum or gas-filled cavities, making them ideal for the nano-thermoelectric bolometers. Indeed, we have demonstrated such a nano-thermoelectric IR bolometer very recently[7].

W. W. Salisbury[8] introduced quarter-wave resistive absorbers, or so called Salibury screens, for radio-frequency (RF) applications in a patent filed in 1943. The idea is to place a conductive layer, which absorbs the RF signal, above a reflecting surface. For maximal absorption, the distance between the reflector and the absorber should be a quarter of the wavelength of the target RF signal, and the sheet resistance of the layer should be equal to the vacuum impedance. Salisbury screens, or quarter-wave resistive absorbers, have been widely studied in RF engineering and optics. In optics this kinds of absorber structure is often called an antiresonant interefence structure[9].

In this paper, we present an analytical model for quarter-wave resistive absorbers. The model can be applied in both RF and optical applications. It is based on the analytical calculations of Fante and McCormack[10]. We compare the analytical model with the results obtained with the transfer-matrix method on the cases of pure conductor and an exemplary IR absorbing metal modeled using experimental optical data. In addition, we show briefly how these kinds of absorbers perform in the IR range. In addition, we present a device model of the nano-thermoelectric IR detector and estimate the full performance of this technology based on the published experimental thermoelectric data on silicon thin and ultrathin films.

## 2. MODELING OF QUARTER-WAVE RESISTIVE ABSORBERS

Figure 2a illustrates the quarter-wave resistive absorber. It consists of an absorbing layer with thickness $t_{abs}$. It is placed above a back reflector. The space between the absorbing layer and the back reflector defines the optical cavity with the depth $d_{cav}$. The optical cavity can be vacuum or gas, or it can be filled by non-absorbing material, which is often called a spacer. The incident optical (or RF) radiation (or signal) passes first through the absorbing layer and then reflects back

from the back reflector to pass through the absorbing layer again. As shown in Fig. 2b, the incident and reflected optical wavelengths interfere and form a standing wave. The absorber works most efficiently when $d_{cav}$ is selected such a way that the antinode of the standing wave is in the absorbing layer.

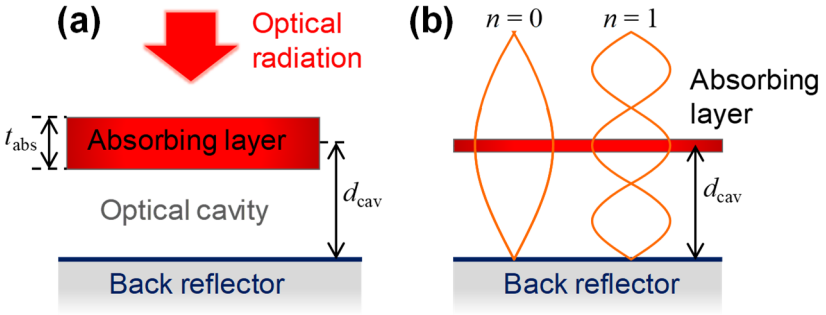


Figure 2. Schematic pictures of a quarter-wave absorber. (a) Cross-section of the absorber structure. The absorbing layer with thickness $t_{abs}$ is placed above a back reflector, which is reflecting the optical radiation. Optical cavity with the depth of $d_{cav}$ is formed between the back reflector and the absorbing layer. (b) Illustration of optical waves in the absorber in the cases corresponding to two absorption peaks with the longest wavelengths, i.e. lowest orders $n$. The optical absorption is strongest when an antinode of the optical wave is on the absorbing layer.

### 2.1 Optical modeling using transfer-matrix method

In the transfer-matrix method[11,12], the modeled structure is divided into slabs of uniform optical media. The propagation and attenuation of optical wave in these slabs and at their boundaries are described and solved in the matrix form. We describe the studied materials with complex refractive index $n_c = n + ik$, which is related to the complex relative electric permittivity $\varepsilon_r$ by $n_c = \sqrt{\varepsilon_r}$. The complex relative electric permittivity of a conducting material is given by $\varepsilon_r = \varepsilon_r' - i\sigma/(\omega\varepsilon_0)$, where $\varepsilon_r'$ is (the real part of) the electric permittivity and $\sigma$ is the electric conductivity of the material, respectively, and $\omega$ is the angular frequency of the optical wave.

### 2.2 Analytical model of quarter-wave resistive absorbers and Salisbury screens

Fante and McCormack[10] have calculated analytically (field) reflection coefficients of various quarter-wave absorber structures. Based on their calculations we present an analytical model for quarter-wave resistive absorbers (i.e. Salisbury screens). The model is valid, when the thickness of the absorbing layer $t_{abs}$ is much smaller than the wavelength of the optical signal, and the back reflector reflects fully the optical waves with the considered wavelengths. The reflection coefficient of a quarter-wave absorber structure without magnetic properties in the absorbing layer is given by

$$\Gamma = \frac{i\left(1 - \frac{Y_{abs}}{Y_0}\right)\sin k_{cav}d_{cav} - \sqrt{\frac{\varepsilon_{cav}}{\mu_{cav}}}\cdot\frac{1}{Y_0}\cos k_{cav}d_{cav}}{i\left(1 + \frac{Y_{abs}}{Y_0}\right)\sin k_{cav}d_{cav} + \sqrt{\frac{\varepsilon_{cav}}{\mu_{cav}}}\cdot\frac{1}{Y_0}\cos k_{cav}d_{cav}} e^{i2k_0 d_{cav}}, \quad (1)$$

where $k_{cav} = k_0\sqrt{\mu_{cav}\varepsilon_{cav}\mu_0^{-1}\varepsilon_0^{-1}}$ is the wavenumber of the optical cavity, $\omega$ the angular frequency, $k_0 = \omega\sqrt{\mu_0\varepsilon_0}$ the vacuum wave number, $Y_0$ is the vacuum admittance, $\mu_0$ the vacuum permeability, and $\varepsilon_0$ the vacuum permittivity, respectively. The vacuum impedance is given by $Z_0 = 1/Y_0 = \sqrt{\mu_0/\varepsilon_0} \approx 376.73\ \Omega$. The optical cavity is described by the depth of the optical cavity $d_{cav}$, magnetic permeability $\mu_{cav}$, and electric permittivity $\varepsilon_{cav}$. The electric surface admittance of the absorbing layer is defined as

$$Y_{abs} = \omega\int_0^{t_{abs}} (\varepsilon_{abs}'' + j\varepsilon_{abs}')\,dz \quad (2)$$

where $z$ is the coordinate in the propagation direction of the electromagnetic wave, and the complex permittivity of the absorbing layer is given by $\varepsilon_{\mathrm{abs}} = \varepsilon'_{\mathrm{abs}} - i\varepsilon''_{\mathrm{abs}}$.

In the classic Salisbury screen absorber, the absorbing layer is purely resistive. We assume that the absorbing material is a pure conductor, i.e. $\varepsilon'_{\mathrm{abs}} = 0$ and $\varepsilon''_{\mathrm{abs}} = \sigma_{\mathrm{abs}}/\omega$, where $\sigma_{\mathrm{abs}}$ is the electric conductivity of the absorbing layer. In this case, eq. (2) yields

$$Y_{\mathrm{abs}} = \frac{1}{R_{\mathrm{sh}}}, \tag{3}$$

Where $R_{\mathrm{sh}} = 1/(\sigma_{\mathrm{abs}} t_{\mathrm{abs}})$ is the sheet resistance of the absorbing layer. In infrared bolometers the optical cavity is often vacuum or filled with gases of electromagnetically similar properties. In the case of vacuum, $\mu_{\mathrm{cav}} = \mu_0$, $\varepsilon_{\mathrm{cav}} = \varepsilon_0$, $k_{\mathrm{cav}} = k_0 = 2\pi/\lambda$, and eqs. (1) ad (3) yield for the absorptance of the ideal quarter-wave resistive absorber

$$A = 1 - |\Gamma|^2 = \frac{4\frac{Z_0}{R_{\mathrm{sh}}}\left[\sin\left(\frac{2\pi d_{\mathrm{cav}}}{\lambda}\right)\right]^2}{\frac{Z_0}{R_{\mathrm{sh}}}\left(\frac{Z_0}{R_{\mathrm{sh}}} + 2\right)\left[\sin\left(\frac{2\pi d_{\mathrm{cav}}}{\lambda}\right)\right]^2 + 1}, \tag{4}$$

where $\lambda$ is the wavelength. Eq. (4) shows that the absorptance is maximized when $\sin\left(\frac{2\pi d_{\mathrm{cav}}}{\lambda}\right) = \pm 1$. Therefore, the wavelengths of the absorption peaks are given by

$$\lambda_{\mathrm{peak}} = \frac{4d_{\mathrm{cav}}}{1 + 2n}, \tag{5}$$

where the order $n$ = 0, 1, 2, 3, …. In the frequency domain the absorption peaks are evenly spaced with spacing $c/(2d_{\mathrm{cav}})$, where $c$ is the speed of light. The lowest frequency peak is at $c/(4d_{\mathrm{cav}})$.

Eqs. (4) and (5) allow the calculation of the characteristics of the quarter-wave resistive absorber. Eq. (4) shows that the full absorption ($A$ = 1) is obtained when $R_{\mathrm{sh}} = Z_0$, i.e. when the absorbing layer is matched to vacuum impedance. The dependence of the absorptance on the sheet resistance of the absorbing layer, $R_{\mathrm{sh}}$, and the impedance matching is determined by $R_{\mathrm{sh}}/Z_0$. Solving eq. (4) at the maximum of the absorption peaks [the condition of eq. (5)] for $R_{\mathrm{sh}}/Z_0$ gives

$$\frac{R_{\mathrm{sh}}}{Z_0} = \frac{A}{2 - A \pm 2\sqrt{1 - A}}. \tag{6}$$

The absorption bands can also be calculated using the same equation. Solving eq. (4) for $\lambda$ gives for the high-wavelength side of the absorption peak ($\lambda_{\mathrm{peak}}$)

$$\lambda_1 = \frac{2\pi d_{\mathrm{cav}}}{\pi n + \arcsin\left(\frac{\sqrt{A_{\mathrm{edge}}}}{\frac{Z_0}{R_{\mathrm{sh}}}\sqrt{\left(4 - 2A_{\mathrm{edge}}\right)\frac{R_{\mathrm{sh}}}{Z_0} - A_{\mathrm{edge}}}}\right)}, \tag{7a}$$

and for the low-wavelength side

$$\lambda_2 = \frac{2\pi d_{\mathrm{cav}}}{\pi(n+1) - \arcsin\left(\frac{\sqrt{A_{\mathrm{edge}}}}{\frac{Z_0}{R_{\mathrm{sh}}}\sqrt{\left(4 - 2A_{\mathrm{edge}}\right)\frac{R_{\mathrm{sh}}}{Z_0} - A_{\mathrm{edge}}}}\right)}, \tag{7b}$$

where $A_{\mathrm{edge}}$ is the absorptance of the peak edge.

### 2.3 Device model of thermoelectric bolometer

In this section, we present the device model of a thermoelectric bolometer, and use it to estimate the device performance. The model is based on a thermal RC circuit[1,4,7,13,14]. The thermoelectric transducer of the bolometer is described by the total Seebeck coefficient

$$S = \frac{\mathrm{d}V}{\mathrm{d}T} = S_p - S_n, \tag{8}$$

where $V$ is the output voltage of the bolometer, $T$ is the absolute temperature of the absorber, and $S_\mathrm{p}$ and $S_\mathrm{n}$ are the Seebeck coefficients of the n- and p-type thermoelectric elements, respectively. The speed of the thermoelectric bolometer is described by thermal time constant given by[4,7,13]

$$\tau = \frac{C_\mathrm{th}}{G_\mathrm{th}}, \tag{9}$$

where $C_\mathrm{th}$ is the thermal capacitance, i.e. the heat capacity, of the bolometer, and $G_\mathrm{th}$ is the thermal conductance of the bolometer (i.e. the thermal conductance between the absorber and the substrate and surroundings). In this work, we neglect the thermal conductance associated with the supporting structures of the bolometer. In this case, the thermal conductance of the bolometer is given by

$$G_\mathrm{th} = G_\mathrm{th,n} + G_\mathrm{th,p}, \tag{10}$$

were $G_\mathrm{th,n} = G_\mathrm{th,sh,n}/N_\mathrm{n}$ and $G_\mathrm{th,p} = G_\mathrm{th,sh,p}/N_\mathrm{p}$ are the thermal conductances of the n- and p-type thermoelectric elements, respectively. Here $N_\mathrm{n}$ and $N_\mathrm{p}$ are the number of squares (i.e. the length-to-width ratios) in the n- and p-type thermoelectric elements. The n- and p-type sheet thermal conductances are given by $G_\mathrm{th,sh,n} = \kappa_\mathrm{n} t_\mathrm{TE}$ and $G_\mathrm{th,sh,p} = \kappa_\mathrm{p} t_\mathrm{TE}$, where $\kappa_\mathrm{n}$ and $\kappa_\mathrm{p}$ are the thermal conductivities of the n- and p-type thermoelectric materials, respectively. Here $t_\mathrm{TE}$ is the thickness of the thermoelectric elements, which is assumed equal for both n- and p-type elements.

In this work, we neglect the heat capacities of the supporting structures and the partial contributions of the thermoelectric elements to the heat capacity. In this case, the heat capacity of the bolometer can be written as

$$C_\mathrm{th} = C_\mathrm{th,abs} + C_\mathrm{th,TE}, \tag{11}$$

where the heat capacity of the absorbing layer is given by $C_\mathrm{th,abs} = c_\mathrm{V,abs} A_\mathrm{abs} t_\mathrm{abs}$, where $c_\mathrm{V,abs}$ is the volumetric heat capacity of the absorbing layer, and $A_\mathrm{abs}$ is the absorber area and the $t_\mathrm{abs}$ thickness of the absorbing layer. The second term in eq. (11) can be omitted if the thermoelectric materials of the thermoelectric elements are not present in the absorber area. Here term $C_\mathrm{th,TE}$ describes the case where the thermoelectric materials cover evenly the whole absorber area. In this case the heat capacity originated from the thermoelectricmaterials is given by $C_\mathrm{th,TE} = c_\mathrm{V,TE} A_\mathrm{abs} t_\mathrm{TE,}$ where $c_\mathrm{V,TE}$ is the effective volumetric heat capacity of the n- and p-type thermoelectric materials.

Below the angular thermal cut-off frequency, $1/\tau$, the voltage responsivity of a thermoelectric bolometer is given by[4,7,13]

$$R_\mathrm{V} = \frac{dV}{dP} = \frac{S\eta}{G_\mathrm{th}}, \tag{12}$$

where $P$ is the incident optical power on the absorber, and $\eta$ is the total optical efficiency of the absorber, which is equal to the absorptance $A$ of absorber[7]

$$\eta = \frac{P_\mathrm{abs}}{P} = \frac{\int A(\lambda) P_\lambda(\lambda) \mathrm{d}\lambda}{\int P_\lambda(\lambda) \mathrm{d}\lambda}, \tag{13}$$

where $P_\mathrm{abs}$ is the absorbed optical power, $A = A(\lambda)$ is the absorptance of the absorber, $P_\lambda(\lambda)$ is the spectral incident optical power at wavelength $\lambda$. In this work, we assume that the spectrum of the incident optical power is such that we can design an absorber with $A(\lambda) = 1$ in the target spectral range. The modeling results of the previous section show that this assumption is reasonable and can be achieved in most cases with the quarter-wave resistive absorbers.

The sensitivity of the bolometer is characterized by (optical) noise-equivalent power (NEP) and specific detectivity $D^*$. The noise of the bolometer comprises of two noise sources, the Johnson-Nyquist noise and the thermal fluctuation noise. The NEP corresponding to the Johnson-Nyquist noise is given by

$$\mathrm{NEP_{JN}} = \frac{\sqrt{4k_\mathrm{B}TR}}{R_\mathrm{V}}, \tag{14}$$

where $k_\mathrm{B}$ is Boltzmann's constant and $R$ the total resistance of the bolometer given by

$$R = R_\mathrm{n} + R_\mathrm{p}, \tag{15}$$

where $R_\mathrm{n} = R_{\mathrm{sh,n}}N_\mathrm{n}$ and $R_\mathrm{p} = R_{\mathrm{sh,p}}N_\mathrm{p}$ are the resistances, $R_{\mathrm{sh,n}} = \rho_\mathrm{n}/t_\mathrm{TE}$ and $R_{\mathrm{sh,p}} = \rho_\mathrm{p}/t_\mathrm{TE}$ the sheet resistances, and $\rho_\mathrm{n}$ and $\rho_\mathrm{p}$ the resistivities of the n- and p-type thermoelectric elements. In this work, we have neglected the contributions of electric contacts and leads to $R$. The NEP corresponding to the thermal fluctuation noise is given by $\mathrm{NEP_{th}} = \sqrt{4k_BT^2G_\mathrm{th}}/\eta$. These noise sources can be combined into total (optical) NEP as[4,7,13]

$$\mathrm{NEP} = \sqrt{\mathrm{NEP_{th}^2} + \mathrm{NEP_{JN}^2}} = \mathrm{NEP_{th}}\sqrt{1 + \frac{1}{\widetilde{ZT}}}, \tag{16}$$

where the effective thermoelectric figure of merit of the bolometer is given by

$$\widetilde{ZT} = \frac{S^2T}{G_\mathrm{th}R}. \tag{17}$$

Finally, the specific detectivity of the bolometer is given by

$$D^* = \frac{\sqrt{A_\mathrm{abs}}}{\mathrm{NEP}}. \tag{18}$$

## 3. RESULTS AND DISCUSSION

### 3.1 Characteristics of ideal quarter-wave resistive absorber

In this section we study the characteristics of an ideal quarter-wave resistive absorber using the analytical model and the transfer-matrix method with pure conductor (constant $\sigma$ and $\varepsilon_r' = 0$). Figure 3 shows the absorptance spectra calculated using the analytical model [eq. (4)] with various values of the ratio of $R_\mathrm{sh}/Z_0$. The graph shows that the absorption spectra consists of peaks, the locations of which are given by eq. (5). In the impedance matched case of $R_\mathrm{sh}/Z_0 = 1$, the absorption peaks reach the maximum absorption.

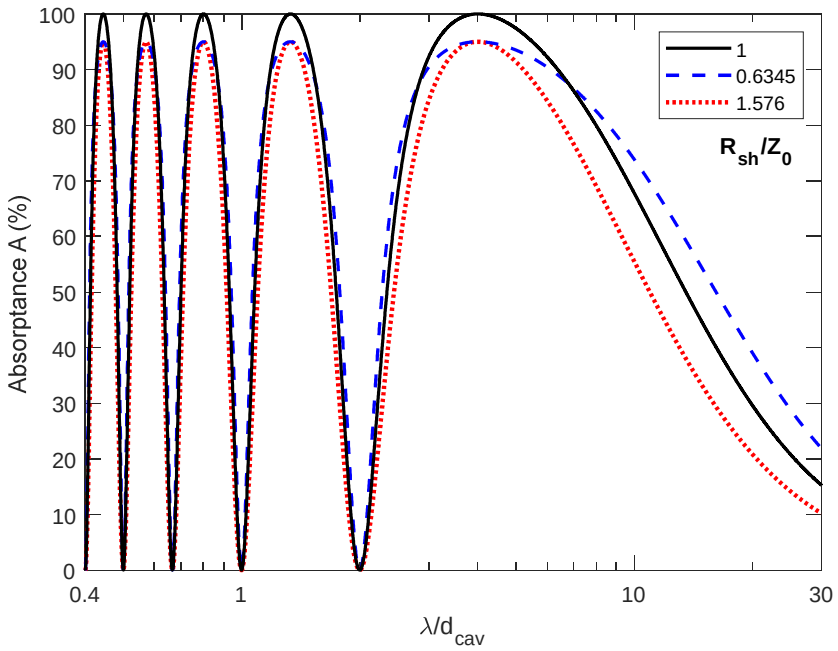


Figure 3. Absorptance spectra of quarter-wave resistive absorber with various values of the normalized sheet resistance $R_{sh}/Z_0$. Calculated using the analytical model [eq. (4)]. The wavelength $\lambda$ is normalized with the depth of the optical cavity $d_{cav}$. The peak positions and the shapes of the peak edges can be calculated using eqs. (5), (7a), and (7b).

The peak with the longest wavelength is the widest one and the widths of the peaks as well as their interspacing becomes smaller as the wavelength decreases. Table 1 lists the calculated peak positions and the full-width-at-half-maximum (FWHM) bandwidths of the corresponding peaks. The 90% and 99% absorption bandwidths of the peaks are listed in Tables A1 and A2 in the Appendix. The absorption peak with the longest wavelength (order $n = 0$) is the widest one with the relative bandwidth of 280%, when the absorptance is 50%. If the absorptance level of 99% is required, the relative bandwidth of the longest-wavelength peak is still as high as 26% (see Table A2). The reason for the narrowing and the change in the spacing can be seen Fig. 2b, which shows that for the longest wavelengths (the lowest orders $n$), a small change in the wavelength has only a minor effect on the position of the antinode in relation to the absorbing layer. In the cases of low-wavelength peaks (high orders $n$), a small change in the wavelength can easily move a node into the absorbing layer, causing the absorptance to collapse.

Table 1. The peak wavelengths ($\lambda_{peak}$), the upper and lower wavelengths ($\lambda_1$ and $\lambda_2$) of the FWHM bands (i.e. 50% edges) of the absorption peaks, and the spectral bandwidths ($\lambda_1 - \lambda_2$) of the absorption peaks of the quarter-wave resistive absorber. Calculated using eqs. (5), (7a), and (7b) with $A_{edge}$ = 50% and $R_{sh}$= $Z_0$. The wavelength values are normalized with respect to the depth of the cavity ($d_{cav}$) or the peak wavelength ($\lambda_{peak}$).

| $n$ | $\frac{\lambda_{peak}}{d_{cav}}$ | $\frac{\lambda_1}{d_{cav}}$ | $\frac{\lambda_2}{d_{cav}}$ | $\frac{\lambda_1 - \lambda_2}{d_{cav}}$ | $\frac{\lambda_1 - \lambda_2}{\lambda_{peak}}$ |
|---|---|---|---|---|---|
| 0 | 4 | 13.55 | 2.346 | 11.21 | 280.1% |
| 1 | 4/3 ≈ 1.333 | 1.743 | 1.008 | 0.6631 | 49.73% |
| 2 | 4/5 = 0.8 | 0.9313 | 0.7012 | 0.2301 | 28.76% |
| 3 | 4/7 ≈ 0.5714 | 0.6354 | 0.5192 | 0.11625 | 20.34% |
| 4 | 4/9 ≈ 0.4444 | 0.4822 | 0.4122 | 0.07004 | 15.76% |
| 5 | 4/11 ≈ 0.3636 | 0.3885 | 0.3417 | 0.04679 | 12.87% |

As Fig. 3 shows, impedance mismatch ($R_{sh} \neq Z_0$) decreases the maximal absorptances of the peaks. In addition to the decrease in the peak maxima, the shape of the spectra changes. Although, in the cases of $R_{sh}/Z_0$ = 0.6345 and $R_{sh}/Z_0$ = 1.576 of Fig. 3 the peak maxima are equal, the bandwidth is larger for the smaller $R_{sh}/Z_0$. Figure 4 shows the dependencies of the absorptances of the peak maxima on the impedance matching $R_{sh}/Z_0$. In spite of the lowering of the absorptance, relatively large impedance mismatches can be allowed. For example, absorptance of 99% can still be reached with the impedance mismatch of ~20%. The absorptance of 90% or higher can be obtained with impedance mismatch between -48% and +93%. The detailed values are listed in Table 2.

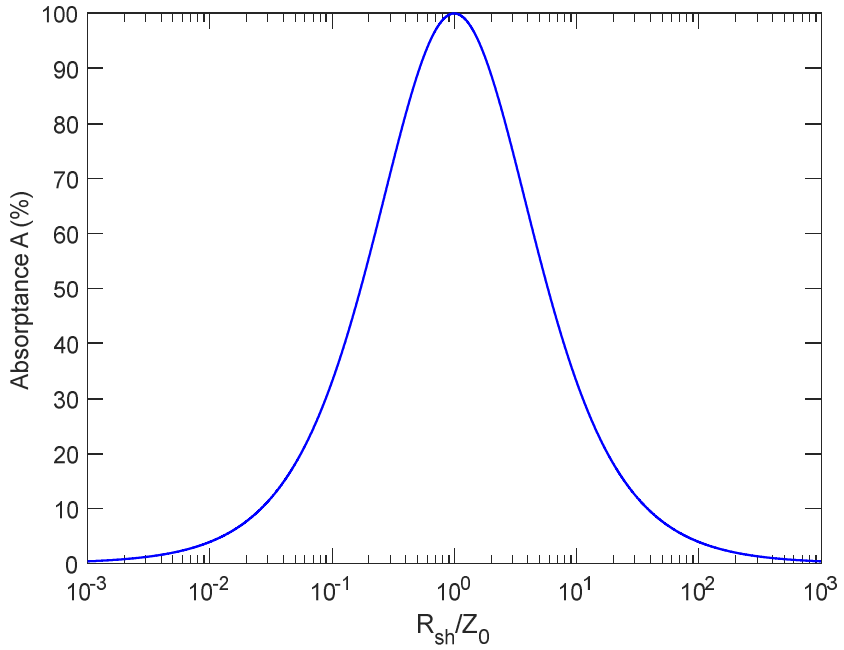


Figure 4. Dependence of absorptance $A$ of the quarter-wave resistive absorber on ratio between the sheet resistance of the absorber $R_{sh}$ and vacuum impedance $Z_0$ when the wavelength of the optical signal is at the maximum of an absorber peak [condition eq. (5)]. Calculated using eq. (6).

Table 2. Dependence of the absorptance on the impedance matching of the absorbing layer. Calculated using eq. (6), which applies under the condition defined by eq. (5).

| **Minimum required value for absorptance *A*** | **Minimum allowed value for $R_{sh}/Z_0$** | **Minimum allowed value for $R_{sh}$ (Ω)** | **Maximum allowed value for $R_{sh}/Z_0$** | **Maximum allowed value for $R_{sh}$ (Ω)** |
|---|---|---|---|---|
| 100% | 1 | 376.7 | 1 | 376.7 |
| 99% | 0.8182 | 308.2 | 1.222 | 460.4 |
| 95% | 0.6345 | 239.4 | 1.576 | 593.7 |
| 90% | 0.5195 | 195.7 | 1.925 | 725.2 |
| 50% | 0.1716 | 64.64 | 5.828 | 2196 |

In the above analysis, we assumed that the back reflector is fully reflecting. The effect of the reflectance of the back reflector on the efficiency of the quarter-wave resistive absorber is shown in Figure 5, which was obtained using the transfer-matrix method with a pure conductor. Fig. 5 shows that the dependence of the absorptance $A$ on the back reflector reflectance is relatively weak. For example, $A$ = 85% is obtained with the reflectance of 50%, and $A$ = 76% with the reflectance of 50%, respectively.

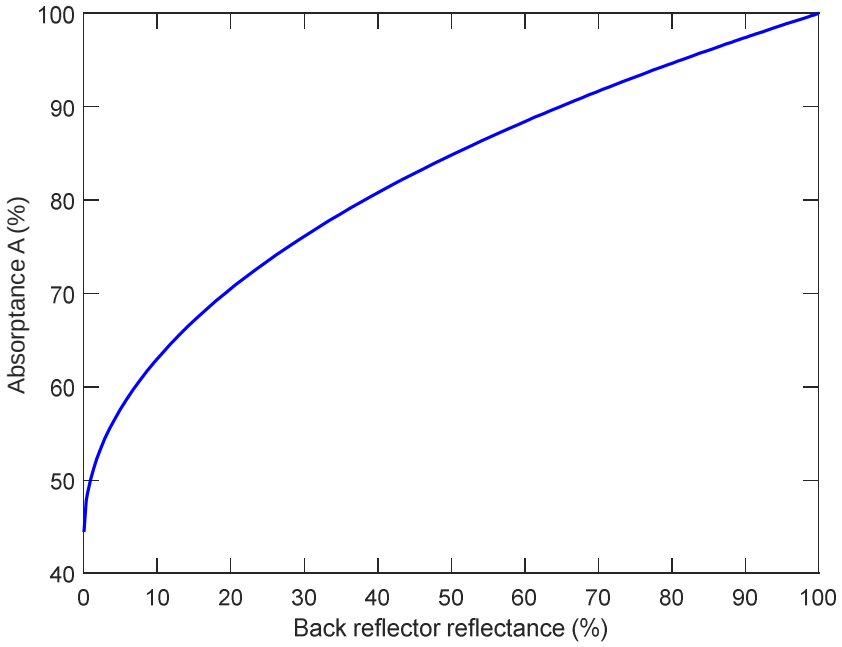


Figure 5. Dependence of absorptance $A$ of the quarter-wave resistive absorber on the reflectivity of the back reflector. Calculated using the transfer-matrix method with the parameter values $d_{cav}$ = 2500 nm, $t_{abs}$ = 10 nm, and $\lambda$ = 10 μm. The absorbing layer is a pure conductor with $R_{sh} = Z_0$, $\sigma = 1/(R_{sh}t_{abs})$, and $\varepsilon_r' = 0$.

### 3.2 Comparison of absorber models

In this section, we compare the analytical and the transfer-matric methods in the case of a long-wavelength IR (LWIR) absorber. Figure 6 shows the comparison of the absorption spectra of a quarter-wave resistive absorber calculated using the analytical model [eq. (4)] and the transfer-matrix method. We have selected metallic $VO_2$[15] as an exemplary material for the absorbing layer. In the calculations, this material was presented both as a pure conductor and using experimental optical data.

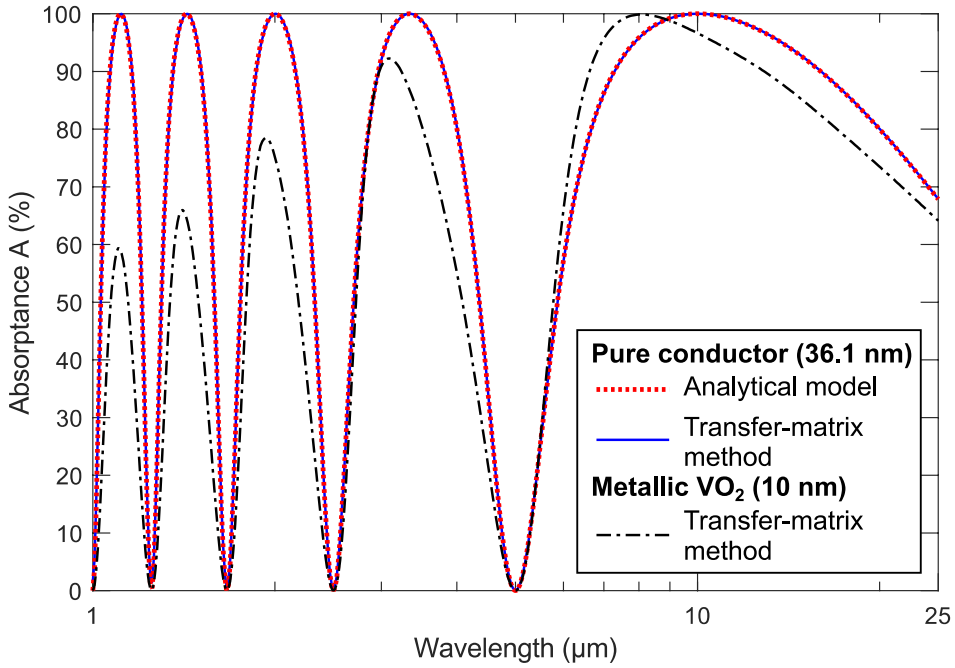


Figure 6. Comparison of absorption spectra of a quarter-wave resistive absorber calculated using the analytical model [eq. (4)] and the transfer-matrix method. The depth of the optical cavity is with $d_{cav}$ = 2500 nm. Here the exemplary absorbing layer is metallic $VO_2$ (sample film 3 in the reference)[15], which modeled either as a pure conductor with the experimental DC electric conductivity $\sigma = 7.35 \cdot 10^4$ S/m, or using experimental $n$ and $k$ data. In the pure conductor case, the thickness of the absorbing layer was set to $t_{abs}$ = 36.1 nm to achieve impedance matching to vacuum [$R_{sh} = 1/(\sigma_{abs} t_{abs}) = Z_0 = 376.73\ \Omega$].

The pure conductor and $VO_2$ spectra are similar with the 0% absorptance peaks (corresponding to destructive interference) at exactly the same locations, and the 100% absorption peaks roughly at the same positions. However, in the $VO_2$ case the absorption peaks are slightly distorted and decay with decreasing wavelength. The distortion is caused by the features of the complex permittivity and the imaginary part of the electric conductivity, which are present in real materials. These are not taken into account in the pure conductor case and in the analytical model. The decay of the absorption peaks is due to the Drude behavior of the metals, where the real part of the electric conductivity starts to decrease at low wavelengths. These effects also result in the fact that the optimal thickness of the absorbing layer is different for the experimental DC electric conductivity and the experimental $n$ and $k$ data. The slight peak distortion in the $VO_2$ case can be compensated by tuning the cavity depth. For example, a $VO_2$ based absorber with 100% absorption at the wavelength of 10 μm can be achieved with the cavity depth of 3075 nm.

In the pure conductor case of Fig. 6, the absorption spectra obtained using the analytical model and the transfer-matrix method are almost identical. At 10 μm both models produce exactly the same results. When the wavelength is decreased, the absorption peaks calculated using the transfer-matrix model shift slightly to lower wavelengths (not visible in the figure). In Fig. 6, the maximum difference between the absorptance predicted by these models is less than 0.015. This difference between the models is caused by the finite thickness of the absorbing layer in the transfer-matrix model.

In overall, the analytical model compares reasonably well with the detailed model based on experimental material data. It is able to describe the main characteristics of a quarter-wave resistive absorber. Therefore, it provides a simple and good start for more detailed optical calculations. Fig. 6 shows also that a quarter-wave resistive absorber based on metallic $VO_2$ and other similar metals can be used as an efficient absorber in the LWIR range.

### 3.3 Modeling of thermoelectric bolometers based on silicon nanomembranes

In this section, we use the device model presented in section 2.3 to estimate the performances of thermoelectric bolometers based on silicon nanomembranes. The device model consists of eqs. (8)-(18), and the key characteristics, the time constant $\tau$ and specific detectivity $D^*$, are given by eqs. (9) and (18). For the bolometer heat capacity $C_{th}$ given by eq. (11), we use two cases: an ideal case where $C_{th}$ is determined only by the absorbing layer [i.e. $C_{th,TE} = 0$ in eq. (11)], and a case where the thermoelectric membrane of the legs cover also the absorber area. The theoretical case of $C_{th,TE} = 0$ has the minimum amount of thermal mass as in this case the heat capacity of the absorbing layer determines $C_{th}$. This case represents the ultimate speed-limit of the bolometer.

The parameter values used in the modeling are listed in Table 3. The thermoelectric elements consist of heavily doped n- and p-type silicon nanomembranes. The absorbing element is a generic 10 nm thick IR absorbing metal with characteristics close to Ti, metallic $VO_2$ and similar metals. For the thermal conductivity $\kappa$ of the Si membrane we use the phenomenological model shown in Fig. 7. For simplicity, we assume equal thermal conductivities and resistivities for n- and p-type, i.e. $\kappa = \kappa_p = \kappa_n$ and $\rho_p = \rho_n$. In the case of dissimilar parameters, the geometries of the n- and p-type thermoelectric legs can be optimized for maximal performance[4].

Table 3. Device model parameters used in calculations.

| Model parameter | Value | Material |
|---|---|---|
| **Thermoelectric transducer** | | |
| Total Seebeck coefficient $S$ | 0.4 mV/K | Heavily doped silicon[4] |
| n-type resistivity $\rho_n$ | 1 mΩcm | Heavily doped silicon |
| p-type resistivity $\rho_p$ | 1 mΩcm | Heavily doped silicon |
| Thermal conductivity $\kappa$ | Model of Fig. 7 | Silicon |
| Volumetric heat capacity of absorbing layer $c_{V,TE}$ | 1.64 MJ/K/m$^3$ | Silicon |
| **Absorber** | | |
| Total optical efficiency of absorber $\eta$ | 100% | Many thin film metals |
| Thickness of absorbing layer $t_{abs}$ | 10 nm | Ti[9], metallic $VO_2$ (see Fig. 6) |
| Volumetric heat capacity of absorbing layer $c_{V,abs}$ | 2.5 MJ/K/m$^3$ | Arbitrary value which is close to many metals including Ti and $VO_2$[16] |

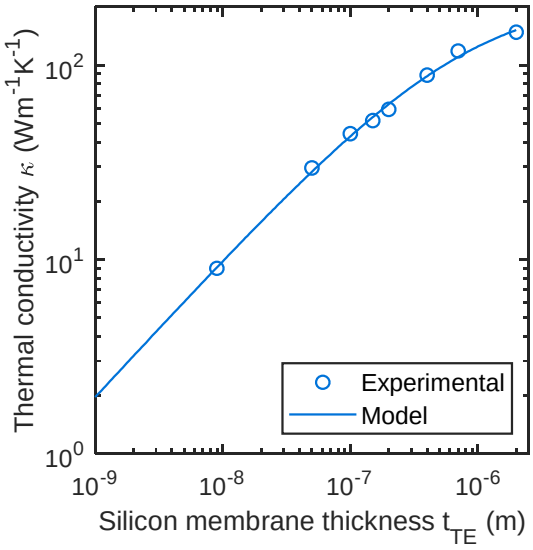


Figure 7. Experimental thermal conductivity $\kappa$ of ultra-thin single-crystalline silicon membranes[17] as a function of membrane thickness. The phenomenological model[13] of $\kappa = \alpha/(1+\beta t^{\gamma})$ with $\alpha$ = 228.4 W/(mK), $\beta$ = 116.0/nm, and $\gamma$ = 0.7149 is fitted to the experimental data.

Figure 8 shows the effect of the silicon nanomembrane thickness $t_{TE}$ on the $D^*$ and $\tau$ of the thermoelectric bolometers with 3 different absorber sizes and leg geometries. As the absorber area $A_{abs}$ determines the amount of radiation collected, $D^*$ increases with increasing $A_{abs}$. Fig. 8 shows that $D^*$ increases rapidly with decreasing $t_{TE}$. As $t_{TE}$ decreases, the thermal conductivity $\kappa$ of the thermoelectric material decreases (see Fig. 7). The increasing of $D^*$ is due to both the decreasing of $G_{th}$ and increasing of $\widetilde{ZT}$ with decreasing $\kappa$ of the thermoelectric material. The direct and indirect effects of $t_{TE}$ are even stronger on $G_{th}$ as it is directly proportional to both $\kappa$ and $t_{TE}$. The dependence of $\tau = C_{th}/G_{th}$ [eq. (9)] is more complex as both $G_{th}$ and $C_{th}$ decrease with decreasing $t_{TE}$ in the case of finite $C_{th,TE}$. Fig. 8 shows that there is a significant potential for decreasing $\tau$ by reducing $C_{th,TE}$. In the case of 20x20 µm$^2$ device with 200 nm Si membrane, the potential for speed improvement is up to one order of magnitude. However, this potential decreases with decreasing $t_{TE}$.

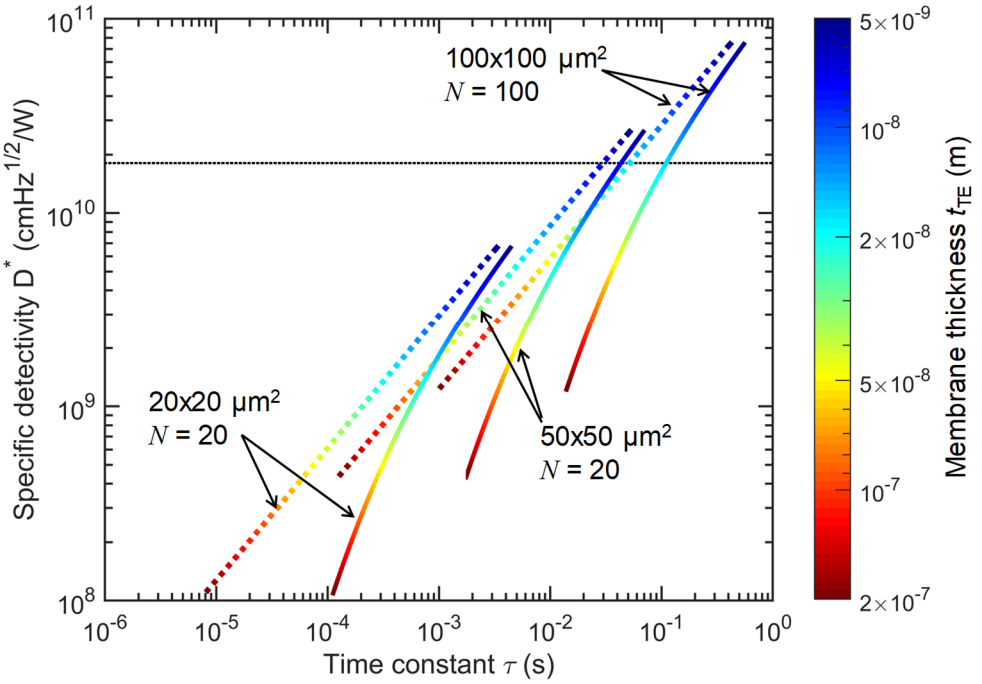


Figure 8. Calculated specific detectivities $D^*$ and thermal time constants $\tau$ of Si-nanomembrane-based thermoelectric bolometers with different absorber areas and leg geometries as functions of the membrane thickness $t_{TE}$. The absorber area $A_{abs}$ and the number of squares in the thermoelectric legs $N = N_n = N_p$ are indicated in the graph. The dotted lines are the case with $C_{th,TE} = 0$ [see eq. (11)]. The parameter values listed in Table 3 and the thermal conductivity model of Fig. 7 were used in the calculations. Theblack line is the background radiation limit for thermal detectors in the full spectrum and half space case at 300 K[18]. Beyond this limit the estimated detector $D^*$ is limited only by the external background noise.

Figures 9 and 10 show the dependencies $D^*$ and $\tau$ on the number of squares in the thermoelectric legs ($N = N_p = N_n$) and the absorber area $A_{abs}$. Both of these geometrical parameters have a similar behavior. $N$ determines $G_{th}$, which determines both $D^*$ and $\tau$. $A_{abs}$ determines $D^*$ and $C_{th}$, which determines $\tau$. Larger $N$ and larger $A_{abs}$ result in higher detectivity $D^*$ and slower speed ($1/\tau$).

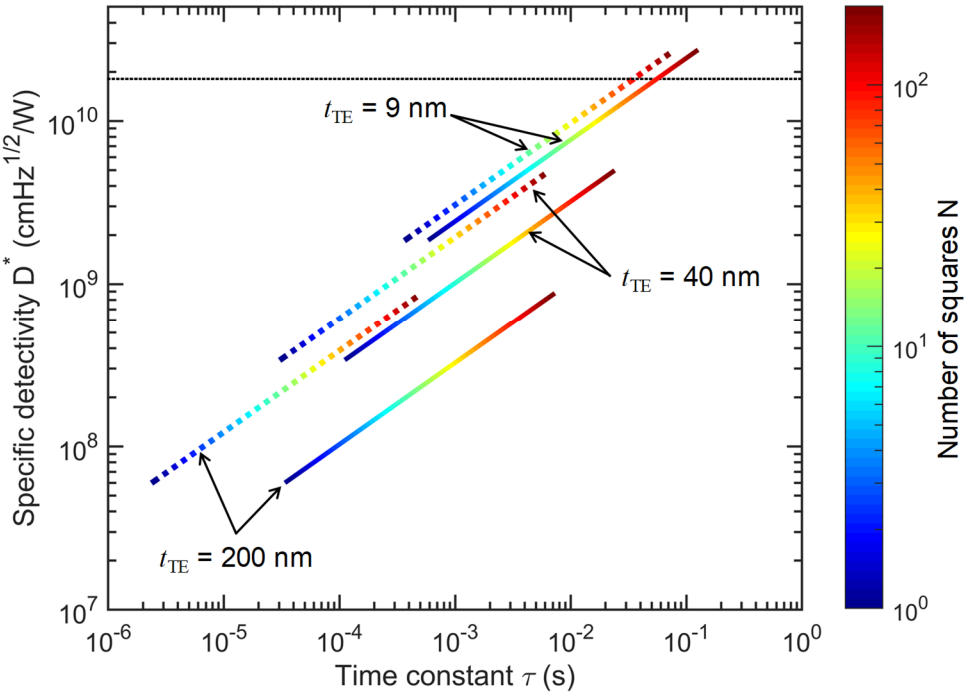


Figure 9. Calculated specific detectivities $D^*$ and thermal time constants $\tau$ of Si-nanomembrane-based thermoelectric bolometers with different membrane thicknesses $t_{TE}$ (indicated) as functions of the number of squares in the thermoelectric legs $N = N_n = N_p$. The absorber area $A_{abs}$ is 50x50 µm$^2$. The dotted lines are the case with $C_{th,TE} = 0$ [see eq. (11)]. The parameter values listed in Table 3 and the thermal conductivity model of Fig. 7 were used in the calculations. The black line is the background radiation limit for thermal detectors in the full spectrum and half space case at 300 K[18]. Beyond this limit the estimated detector $D^*$ is limited only by the external background noise.

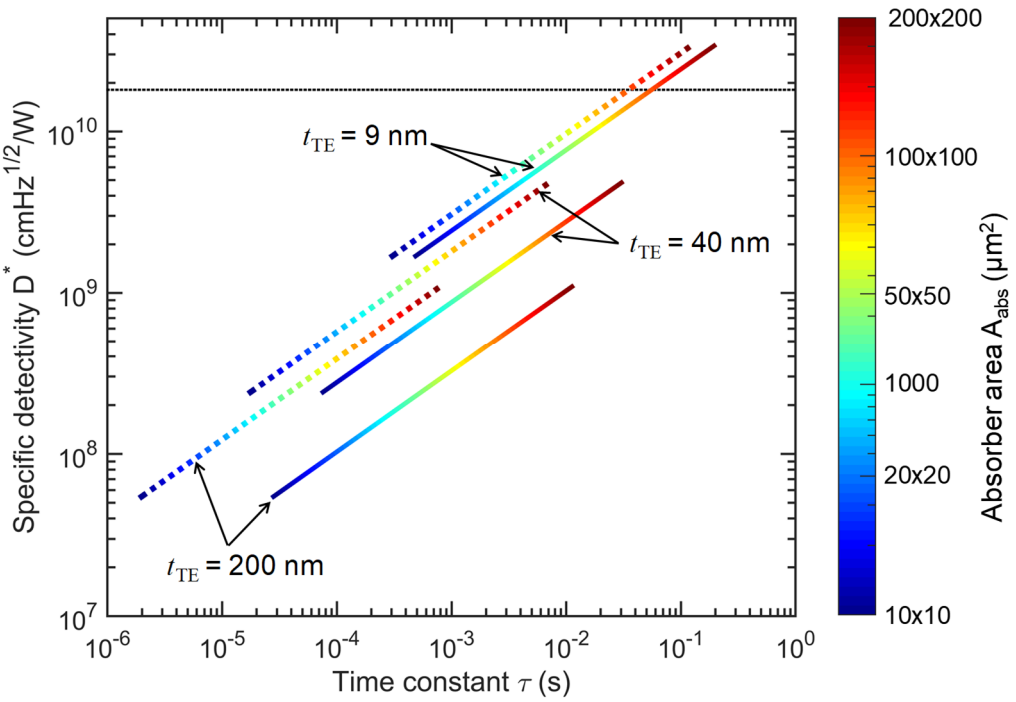


Figure 10. Calculated specific detectivities $D^*$ and thermal time constants $\tau$ of Si-nanomembrane-based thermoelectric bolometers with different membrane thicknesses $t_{TE}$ (indicated) as functions of the area of the absorber $A_{abs}$. The number of squares is $N = N_n = N_p = 20$. The dotted lines are the case with $C_{th,TE} = 0$ [see eq. (11)]. The parameter values listed in Table 3 and the thermal conductivity model of Fig. 7 were used in the calculations. The black line is the background radiation limit for thermal detectors in the full spectrum and half space case at 300 K[18]. Beyond this limit the estimated detector $D^*$ is limited only by the external background noise.

## 4. CONCLUSIONS

We have shown that silicon and metal nanomembranes can be used as high-performance active materials of thermoelectric bolometers. We have very recently demonstrated an experimental LWIR detector based on these materials[7]. We estimated that the nano-thermoelectric bolometer technology can reach 1–2 orders of magnitude higher detectivities and 1–3 orders of magnitude higher speeds than those of the state-of-the-art thermal detectors. In addition, we have presented an analytical model for quarter-wave resistive absorbers, and shown that when equipped with thin-film metals these kinds of absorbers can be used as efficient IR absorbers in bolometers. The analytical model compares reasonably well with the results obtained using the transfer-matrix method with experimental optical data. It provides a simple and good start for more detailed optical calculations.

## ACKNOWLEDGEMENTS

This work has been financially supported by Business Finland co-innovation project RaPtor (No. 6030/31/2018), European Union Seventh Framework Programme (Grant Agreement No. 604668, project QUANTIHEAT), European Union Future and Emerging Technologies (FET) Open under Horizon 2020 programme (Grant Agreement No. 766853, project EFINED), and the Academy of Finland (Grants No. 295329 and 314447). The work of Jonna Tiira was supported by Academy of Finland (Grant No. 324838). Fruitful discussions with Markku Ylilammi and Arto Hujanen are gratefully acknowledged.

## APPENDIX

Table A1. Peak wavelengths ($\lambda_{peak}$), the upper and lower wavelengths ($\lambda_1$ and $\lambda_2$) of the 90% bands (i.e. 90% edges) of the absorption peaks, and the spectral bandwidths ($\lambda_1 - \lambda_2$) of the absorption peaks of the quarter-wave resistive absorber. Calculated using eqs. (5), (6a), and (6b) with $A_{edge}$ = 90% and $R_{sh}$= $Z_0$. The wavelength values are normalized with respect to the depth of the cavity ($d_{cav}$) or the peak wavelength ($\lambda_{peak}$).

| $n$ | $\frac{\lambda_{peak}}{d_{cav}}$ | $\frac{\lambda_1}{d_{cav}}$ | $\frac{\lambda_2}{d_{cav}}$ | $\frac{\lambda_1 - \lambda_2}{d_{cav}}$ | $\frac{\lambda_1 - \lambda_2}{\lambda_{peak}}$ |
|---|---|---|---|---|---|
| 0 | 4 | 6.393 | 2.911 | 3.483 | 87.07% |
| 1 | 4/3 ≈ 1.333 | 1.523 | 1.185 | 0.3380 | 25.35% |
| 2 | 4/5 = 0.8 | 0.8647 | 0.7443 | 0.1205 | 15.06% |
| 3 | 4/7 ≈ 0.5714 | 0.6037 | 0.5424 | 0.06129 | 10.73% |
| 4 | 4/9 ≈ 0.4444 | 0.4637 | 0.4267 | 0.03704 | 8.333% |
| 5 | 4/11 ≈ 0.3636 | 0.3764 | 0.3517 | 0.02478 | 6.814% |

Table A2. Peak wavelengths ($\lambda_{peak}$), the upper and lower wavelengths ($\lambda_1$ and $\lambda_2$) of the 99% bands (i.e. 99% edges) of the absorption peaks, and the spectral bandwidths ($\lambda_1 - \lambda_2$) of the absorption peaks of the quarter-wave resistive absorber. Calculated using eqs. (5), (6a), and (6b) with $A_{edge}$ = 99% and $R_{sh}$= $Z_0$. The wavelength values are normalized with respect to the depth of the cavity ($d_{cav}$) or the peak wavelength ($\lambda_{peak}$).

| $n$ | $\frac{\lambda_{peak}}{d_{cav}}$ | $\frac{\lambda_1}{d_{cav}}$ | $\frac{\lambda_2}{d_{cav}}$ | $\frac{\lambda_1 - \lambda_2}{d_{cav}}$ | $\frac{\lambda_1 - \lambda_2}{\lambda_{peak}}$ |
|---|---|---|---|---|---|
| 0 | 4 | 4.578 | 3.552 | 1.0266 | 25.67% |
| 1 | 4/3 ≈ 1.333 | 1.392 | 1.279 | 0.1125 | 8.434% |
| 2 | 4/5 = 0.8 | 0.8207 | 0.7803 | 0.04044 | 5.055% |
| 3 | 4/7 ≈ 0.5714 | 0.5819 | 0.5613 | 0.02062 | 3.609% |
| 4 | 4/9 ≈ 0.4444 | 0.4508 | 0.4583 | 0.01247 | 2.806% |
| 5 | 4/11 ≈ 0.3636 | 0.3679 | 0.3595 | 0.008350 | 2.296% |

## REFERENCES


[1] Richards, P. L., "Bolometers for infrared and millimeter waves," Journal of Applied Physics **76**(1), 1–24 (1994).

[2] Langley, S. P., "The Bolometer and Radiant Energy," Proceedings of the American Academy of Arts and Sciences **16**, 342–358 (1881).

[3] Shchepetov, A., Prunnila, M., Alzina, F., Schneider, L., Cuffe, J., Jiang, H., Kauppinen, E. I., Sotomayor Torres, C. M. and Ahopelto, J., "Ultra-thin free-standing single crystalline silicon membranes with strain control," Appl. Phys. Lett. **102**(19), 192108 (2013).

[4] Varpula, A., Timofeev, A. V., Shchepetov, A., Grigoras, K., Hassel, J., Ahopelto, J., Ylilammi, M. and Prunnila, M., "Thermoelectric thermal detectors based on ultra-thin heavily doped single-crystal silicon membranes," Appl. Phys. Lett. **110**(26), 262101 (2017).

[5] Varpula, A., Grigoras, K., Tappura, K., Timofeev, A. V., Shchepetov, A., Hassel, J., Ahopelto, J. and Prunnila, M., "Silicon Based Nano-Thermoelectric Bolometers for Infrared Detection," Proceedings of SPIE **2**, 894 (2018).

[6] Neogi, S., Reparaz, J. S., Pereira, L. F. C., Graczykowski, B., Wagner, M. R., Sledzinska, M., Shchepetov, A., Prunnila, M., Ahopelto, J., Sotomayor-Torres, C. M. and Donadio, D., "Tuning Thermal Transport in Ultrathin Silicon Membranes by Surface Nanoscale Engineering," ACS Nano **9**(4), 3820–3828 (2015).
[7] Varpula, A., Tappura, K., Tiira, J., Grigoras, K., Ahopelto, J. and Prunnila, M., "Nano-Thermoelectric Infrared Bolometer," arXiv:1912.12868 [cond-mat, physics:physics] (2019).
[8] Salisbury, W. W., "Absorbent body for electromagnetic waves," U. S. Patent 2,599,944 (1952).
[9] Talghader, J. J., Gawarikar, A. S. and Shea, R. P., "Spectral selectivity in infrared thermal detection," Light Sci Appl **1**(8), e24–e24 (2012).
[10] Fante, R. L. and McCormack, M. T., "Reflection properties of the Salisbury screen," IEEE Trans. Antennas Propagat. **36**(10), 1443–1454 (1988).
[11] Katsidis, C. C. and Siapkas, D. I., "General transfer-matrix method for optical multilayer systems with coherent, partially coherent, and incoherent interference," Appl. Opt., AO **41**(19), 3978–3987 (2002).
[12] Born, M. and Wolf, E., [Principles of Optics: Electromagnetic Theory of Propagation, Interference and Diffraction of Light], Elsevier (2013).
[13] Varpula, A., Timofeev, A. V., Shchepetov, A., Grigoras, K., Ahopelto, J. and Prunnila, M., "Thermoelectric bolometers based on silicon membranes," Proceedings of SPIE **10246**, 102460L (2017).
[14] Dillner, U., Kessler, E. and Meyer, H.-G., "Figures of merit of thermoelectric and bolometric thermal radiation sensors," J. Sens. Sens. Syst. **2**(1), 85–94 (2013).
[15] Wan, C., Zhang, Z., Woolf, D., Hessel, C. M., Rensberg, J., Hensley, J. M., Xiao, Y., Shahsafi, A., Salman, J., Richter, S., Sun, Y., Qazilbash, M. M., Schmidt-Grund, R., Ronning, C., Ramanathan, S. and Kats, M. A., "On the Optical Properties of Thin-Film Vanadium Dioxide from the Visible to the Far Infrared," Annalen der Physik **531**(10), 1900188 (2019).
[16] Hamaoui, G., Horny, N., Gomez-Heredia, C. L., Ramirez-Rincon, J. A., Ordonez-Miranda, J., Champeaux, C., Dumas-Bouchiat, F., Alvarado-Gil, J. J., Ezzahri, Y., Joulain, K. and Chirtoc, M., "Thermophysical characterisation of VO2 thin films hysteresis and its application in thermal rectification," Sci Rep **9**(1), 8728 (2019).
[17] Chávez-Ángel, E., Reparaz, J. S., Gomis-Bresco, J., Wagner, M. R., Cuffe, J., Graczykowski, B., Shchepetov, A., Jiang, H., Prunnila, M., Ahopelto, J., Alzina, F. and Sotomayor Torres, C. M., "Reduction of the thermal conductivity in free-standing silicon nano-membranes investigated by non-invasive Raman thermometry," APL Materials **2**(1), 012113 (2014).
[18] Kruse, Paul. W., "A comparison of the limits to the performance of thermal and photon detector imaging arrays," Infrared Physics & Technology **36**(5), 869–882 (1995).